# Sophisticated rGO synthesis and pre-lithiation unlocking full-cell lithium-ion battery high-rate performances

Benoît Denis Louis Campéon[a], Yumi Yoshikawa[a], Takashi Teranishi[a], Yuta Nishina[a,b*]

[a]*Graduate School of Natural Science and Technology, Okayama University, 3-1-1 Tsushima-naka, kita-ku, Okayama, 700-8530, Japan.*

[b]*Research Core for Interdisciplinary Sciences, Okayama University, 3-1-1 Tsushima-naka, kita-ku, Okayama, 700-8530, Japan.*

** Corresponding authors:*

*Email:* nisina-y@cc.okayama-u.ac.jp (Y. Nishina)

## Abstract

For the application to portable devices and storage of renewable energies, high-performance lithium-ion batteries are in great demand. To this end, the development of high-performance electrode materials has been actively investigated. However, even if new materials exhibit high performance in a simple evaluation, namely half-cell tests, it is often impossible to obtain satisfactory performance with an actual battery (full cell). In this study, the structure of graphene analogs is modified in various ways to change crystallinity, disorder, oxygen content, electrical conductivity, and specific surface area. These graphene analogs are evaluated as negative electrodes for lithium-ion batteries, and we found reduced graphene oxide prepared by combination of chemical reduction and thermal treatment was the optimum. In addition, a full cell is fabricated by combining it with $LiCoO_2$ modified with $BaTiO_3$, which is applicable to high-speed charge-discharge cathode material developed in our previous research. In general, pre-lithiation is performed for the anode when assembling full cells. In this study, we optimized a "direct pre-lithiation" method in which the electrode and lithium foil were in direct contact before assembling a full cell, and created a lithium-ion battery with an output of 293 Wh $kg^{-1}$ at 8,658 W $kg^{-1}$.

*Keywords:* graphene, lithium-ion battery, full-cell, $LiCoO_2$, high-rate

## 1. Introduction

The progress of worldwide energy consumption based on fossil energy has a disastrous impact on the environment for decades. In this context, the transition of fossil energy production toward renewable resources is recently getting intense consideration. However, due to its intermittency, an efficient electric energy storage system is required before its democratization. Among energy storage devices, lithium-ion batteries (LIBs) have arisen as the most promising since its inception in

1976.[1,2] LIBs have received considerable attention due to their high specific capacity, long cycle life, and relatively low environmental impact.[3–6]

In the past few decades, tremendous efforts have been made to develop high-performance electrode materials. Materials with low working potentials, such as Si, Ge, and Sn, have been investigated as anode materials due to their high capacity.[7–9] However, all of them lack in rate capability and stability induced by significant volume expansion.[10] Carbon-based materials, such as graphite and hard carbon, present even lower working potentials.[11] Carbon-based materials show excellent stability due to their relatively limited volume expansion;[12,13] however, compared to Si, Ge, and Sn, they have a lower capacity. The carbon-based materials also suffer from slow rate capability due to the slow intercalation process. In recent years, graphene-based materials have emerged as a solution to improve both the capacity and capability performances of anode materials for LIBs, Li-S batteries, and supercapacitors.[14–18] Amidst the high working potential materials, $LiCoO_2$ became by far the most popular layered transition metal oxide for the cathode. It has a high theoretical capacity of 274 mAh $g^{-1}$ and limited self-discharge; in contrast, $LiCoO_2$ typically has limited cyclability and poor high rate capability.[19,20] To solve these problems, the deposition of $Al_2O_3$ layer *via* atomic layer deposition technic on $LiCoO_2$ was generally applied, improving both the cyclability and rate performances.[21–23] We previously reported the stable and high rate capability cathode material composed of $BaTiO_3$ decorated $LiCoO_2$ (BTO-LCO) prepared by a simple sol-gel route.[24,25] We experimentally proved the incorporated artificial dielectric layer promotes the Li migration at the triple-phase, namely BTO-LCO-electrolyte, interface.

In the past researches, anode and cathode were often separately evaluated by assembling half-cell using Li foil as a counter electrode. But, the technological transfer from half-cell to full-cell is limited in performances due to the maladjusted choice of the anode that lacks in stability, cyclability, and rate capability. Combined with our specially designed high rate performance cathode (BTO-LCO), graphene has the potential to solve those problems due to its flexibility limiting cracking during cycling, high capacity, excellent cyclability, and high rate capability;[26–28] however, a clear guideline for the optimization of graphene structure for LIBs has not been provided.

Herein, we design various graphene analogs as anode for LIBs by reducing graphene oxide (GO) using chemical, thermal, and microwave reduction methods. The graphene analogs are evaluated by half-cell using Li foil as a counter electrode, then by full-cell using BTO-LCO cathode and graphene anode. The results demonstrate the successful technology transfer from high-performance cathode half-cells toward higher full-cell performance indicating the most appropriate graphene synthesis route for full cell LIBs.

## 2. Experimental Section

### 2.1 Materials

$KMnO_4$, $H_2SO_4$, 30% aq. $H_2O_2$, and hydrazine hydrate were purchased from Wako Pure Chemical Industries, Ltd. All the chemicals were used directly without further purification.

### 2.2 Characterization instrumentation

Elemental analyses were performed by PERKINELMER 2400II. Freeze-dried of GO was performed by ADVANTEC DRZ350WC. XPS was measured by JPS-9030 with a pass energy of 20 eV. The crystalline structure of samples was characterized by X-ray diffraction (XRD) using a PANalytical Co. X' part PRO using Cu Kα radiation (λ= 1,541 Å) in the 2θ range of 5–75°. The operating tube current and voltage were 30 mA and 40 kV, respectively. The data was collected at the step size of 0.017°, and the type of scan was continuous. The morphology was measured by transmission electron microscopy (TEM) JEOL JEM-2100F, while the functional groups on the surface of the prepared materials were recorded by Fourier transform infrared spectrometer (FT-IR SHIMADZU IR Tracer 100). The samples for FT-IR were dried and mixed with KBr, and then pressed up to 1.3 mm-diameter pellets.

### 2.3 Preparation of samples for elemental analysis

GO is hydrophilic, and adsorb ca. 10 wt% of water by exposing air. We dried GO and rGOs under vacuum at 50 °C for three days.

### 2.4 Li-ion battery anode sheets preparation

The working electrodes were made of active material (rGO), conductive material (acetylene black), and binder (Polyvinylidene fluoride) in a weight ratio of 7:2:1 by using N-Methyl-2-pyrrolidone as a solvent and a copper foil as the current collector. In order to obtain the homogeneous active and conductive material powder, both materials were mixed in a distilled water-ethanol solution (v/v, 1/1). After mixing, the solution was filtered using Merck Millipore JAWP04700 filter. The powder was freeze and then freeze-dry under vacuum at 30 °C for 48 h. The dry powder was set into ball-milling for 30 min at 300 RPM to reduce the particle size. Then the powder was at first mixed with NMP to obtain a homogeneous slurry and then with the binder. The slurry (active material, conductive material, binder) was spread on a copper foil using a Doctor blade (100 μm thickness). The sheet was dried under vacuum at room temperature for 24 h and in air at 120 °C for 20 min. Finally, the diameter of 15.95 mm sheets was punched and pressed.

## 2.5 Coin cells assembling

The CR2032 coin cells were assembled in an argon-filled glove box using metallic lithium as the counter electrode with a Whatman 1823-257 as a separator and 70 µL electrolyte. The electrolyte was 1 M $L^{-1}$ $LiPF_6$ dissolved in a mixture of ethylene carbonate (EC), diethyl carbonate (DEC) (v/v, 3/7).

## 2.6 Battery cycling

The charge and discharge cycling tests were performed using a multi-channel battery tester (580 8 channel Battery Cycler Scribner Associates Incorporated).

## 2.7 Synthesis

The anode materials, graphene analogs, were synthesized from graphite, through its consecutive oxidation, exfoliation, and reduction. Oxidation and exfoliation of graphite were performed by our modified Hummers' method to obtain 0.83 wt% graphene oxide (GO) dispersion in water.[29] Natural flake graphite (3.0 g) was stirred in 95% H2SO4 (75 mL). KMnO4 (9.0 g) was gradually added to the solution keeping the temperature <10 °C. The mixture was then stirred at 35 °C for 2 h. The resulting mixture was diluted by water (75 mL) under vigorous stirring and cooling so that temperature does not exceed 50 °C. The suspension was further treated by 30% aq. $H_2O_2$ (7.5 mL). The resulting graphite oxide suspension was purified by centrifugation with water until neutralization, and freeze-dried.

Then, the as-prepared materials were firstly chemically reduced using hydrazine (62.5 μL $g^{-1}$ and 1 mL $g^{-1}$), hydrazine scavenges oxygen functional groups and breakdown into $N_2H_2$ and $H_2O$ to produce reduced graphene oxide (rGO) with the oxygen content of 39 wt.% and 14 wt.%, termed as $HrGO_{39}$ and $HrGO_{14}$, respectively.[29–33] Next, both HrGOs were further reduced by heating in a tube furnace or microwave reactor. In these thermal treatments, oxygen functional groups and graphene decomposes into CO and $CO_2$ gases.[34–36] In the tube furnace, the samples were heated under $N_2$ from 0 to 300 °C in 3 hours, 300 to 1,000 °C in 35 minutes, and kept at 1,000 °C for 3 hours; samples were named $HrGO_{XT}$ (X= 39 or 14). For microwave treatment, the samples were exposed to 750 W microwave under $N_2$ for 5 seconds, reaching 1,000 °C within 2 seconds; samples were named $HrGO_{XMW}$ (X= 39 or 14). In the case of $HrGO_{39MW}$, microwave treatment results in fast and large CO and $CO_2$ generation inducing an enormous pressure between graphene layers resulting in their exfoliation and in the increase of their pore size diameter (Table 1).

## 3. Results and discussion

### 3.1 Characterization

The structural analyses of graphene analogs were performed. X-ray diffraction (XRD) patterns (Fig. 1a and Supplementary Fig. S1) showed the homogeneous expansion of interlayer distance of graphite from 0.34 nm to 0.88 nm by oxidation (Fig. 1ai and Supplementary Fig. S1). A mild chemical reduction slightly narrowed the interlayer distance of $HrGO_{39}$ to 0.79 nm (Fig. 1aii), while substantial chemical reduction caused amorphization of $HrGO_{14}$ (Fig. 1av). The thermal reduction at 1,000 °C for 3 hours provided similar amorphous material (Fig. 1aiii and 1avi). After microwave treatment, peaks at 26 ° became sharper, suggesting partial graphitization (Fig. 1aiv and 1avii), while the intensity of $HrGO_{XMW}$ remains 60 times lower than the original graphite (Supplementary Fig. S1). Interestingly, an intensified peak at 43° appeared for $HrGO_{xT}$, indicating that a short-range order in stacked graphene layers could only be obtained through a slow heating process.[37]

Raman spectra (Fig. 1b and Supplementary Fig. S2) were measured to confirm the degree of the defect (intensity ratio of D band and G band; $I_D/I_G$) and the formation of a few-layer (shape of 2D band).[38] Through the graphite oxidation into GO, the $I_D/I_G$ changes from 0.1 to 1.1, and its 2D band became symmetrical, indicating the formation of defects and few-layer material, respectively. After reduction by hydrazine, the $I_D/I_G$ values of $HrGO_{39}$ and $HrGO_{14}$ were 1.1 and 1.4, respectively, indicating the presence of large amounts of defect and disorder.[29,38] After the further reduction in a tube furnace, both $HrGO_{39T}$ and $HrGO_{14T}$ showed an $I_D/I_G$ value of 1.4. The microwave treatment of HrGOs did not affect to the $I_D/I_G$ values of $HrGO_{39MW}$ and $HrGO_{14MW}$. These results indicate the limited defect healing effects of these treatments.

Morphological observation of rGOs was performed by SEM and TEM analyses (Fig. 1c and Supplementary Fig. S3, S4). Both analyses well match with our previous results, where we have confirmed that a high oxygen content GO, such as $HrGO_{39}$, preserved the single-layer nature while a lower oxygen content GO, such as $HrGO_{39MW}$, $HrGO_{14}$, $HrGO_{14T}$, $HrGO_{14MW}$, wrinkled and stacked.[29]

Elemental analysis of as-prepared samples (Table 1 and Supplementary Table S1 ) shows the formation of oxygen functional groups through oxidation; the oxygen content increased from 1.9 wt.% to 47.6 wt.%.[29] After chemical reduction, the oxygen content decrease reaching 39.1 wt.% and 14.4 wt.% for $HrGO_{39}$ and $HrGO_{14}$, respectively. The microwave treatment resulted in 4.8 wt.% and 6.5 wt.% for $HrGO_{39MW}$ and $HrGO_{14MW}$, respectively, while the tube furnace treatment resulted in 2.9 wt.% and 5.5 wt.% for $HrGO_{39T}$ and $HrGO_{14T}$ respectively. The higher oxygen content HrGO was more efficiently reduced. We believe that the reduction was accelerated by CO originated from oxygen functional groups.[34]

X-ray photoelectron spectroscopy (XPS) was conducted to identify oxygen functional groups (Fig. 1di and Supplementary Fig. S5). The narrow C 1s spectra of GO showed the presence of C-OH (286.5 eV), C-O-C (287.1 eV), C=O (288.2 eV), and

C(=O)O (289.2 eV) upon oxidation, and the removal of C-OH and C-O-C was observed upon reduction steps. As C=O groups remained nearly the same amount after reduction, its superior stability toward reduction methods was recognized.[39]

The electroconductivity was measured by a four-point probe method (Table 1). GO was not sufficiently conductive to be measured, but after mild and strong chemical reductions, the conductivity increased to $7.7\times10^{-2}$ and $2.1\times10^{3}$ S $m^{-1}$, respectively. After tube furnace treatment, the conductivity increased up to $5.6\times10^{3}$ and $4.4\times10^{3}$ S $m^{-1}$ for $HrGO_{39T}$ and $HrGO_{14T}$, respectively. These results denote the correlation between the increase of the conductivity and the decrease of oxygen functional group of graphene. The microwave treatment also modified the conductivity to $4.0\times10^{2}$ and $1.7\times10^{3}$ S $m^{-1}$ for $HrGO_{39MW}$ and $HrGO_{14MW}$, respectively, yet the values were lower than expected. This is caused by the morphology of $HrGO_{XMW}$; the $HrGO_{XMW}$ are a tough and sponge-like structure, making it difficult to form pellets for electroconductivity measurement. Therefore, electron conductivity may be underestimated for $HrGO_{XMW}$.

Finally, the porous structure and the specific surface areas (SSA) of all samples were investigated by nitrogen isothermal absorption. The results are summarised in Table 1. The adsorption-desorption isotherm (Fig. 1e,f) of all samples shows a type IV nitrogen adsorption with a capillary condensation step and a hysteresis loop between the adsorption and desorption, which correspond to a mesoporous material. The SSA was evaluated by Brunauer–Emmett–Teller (BET) method for all rGOs (Table 1). Chemically reduced rGOs displayed higher SSA as the hydrazine amount was increased, reaching 88 $m^2$ $g^{-1}$ and 217 $m^2$ $g^{-1}$ for $HrGO_{39}$ and $HrGO_{14}$, respectively. These results suggest the presence of oxygen functional groups limits $N_2$ to access interlayer spaces.[40,41] $HrGO_{14}$ has a medium amount (14.4 wt%) of oxygen and wrinkled 2D structure (Supplementary Figure S3d, 4d), expressing a SSA of 217 $m^2$ $g^{-1}$. The tube furnace treatment slowly removes the oxygen functional groups preserving the wrinkled 2D structure of $HrGO_{14}$ (Supplementary Figure S3e, S4e), resulting in SSA improvement up to 422 $m^2$ $g^{-1}$ due to the formation of point defects by releasing CO and $CO_2$.[42] The microwave treatment quickly removes the oxygen functional groups preserving the wrinkled 2D structure of $HrGO_{14}$ (Supplementary Figure S3f, S4f), resulting in SSA improvement to 333 $m^2$ $g^{-1}$, but less than that with the tube furnace method due to the repair of graphene defects by microwave.[43] $HrGO_{39}$ has a large amount (39.1 wt%) of oxygen and flat 2D structure (Supplementary Figure S3a, S4a), expressing a small SSA of 88 $m^2$ $g^{-1}$. The tube furnace treatment slowly removes the oxygen functional groups preserving the flat 2D structure of $HrGO_{39}$ (Supplementary Figure S3b, S4b), resulting in a small SSA improvement to 93 $m^2$ $g^{-1}$. The microwave treatment explosively removes the large amount of oxygen functional groups of $HrGO_{39}$, resulting in exfoliated wrinkled 2D structure (Supplementary Figure S3c, S4c), and large SSA improvement up to 532 $m^2\ g^{-1}$. This last result indicates that to obtain a large SSA rGO needs to have both low oxygen content and a wrinkled 2D structure.

The pore size distribution was evaluated by Barrett-Joyner-Halenda (BJH) method for all rGOs (Supplementary Fig. S6 and Table 1). The results indicate that the chemical reduction can generate mesopores, reaching a pore volume of 0.057 and 0.354 $cm^3\ g^{-1}$ for $HrGO_{39}$ and $HrGO_{14}$, respectively. The results for thermal reduction of those samples indicate the accentuation of the mesopore amount. For $HrGO_{14}$, the reduction by furnace method is more effective than the microwave method, reaching 0.662 and 0.592 $cm^3\ g^{-1}$ for $HrGO_{14MW}$ and $HrGO_{14MW}$, respectively. For $HrGO_{39}$, the reduction by microwave method is more effective than the furnace method, reaching a pore volume of 3.512 and 0.111 for $HrGO_{39MW}$ and $HrGO_{39T}$, respectively. The drastic increase of pore volume for $HrGO_{39MW}$ is correlated with the formation of macropores resulting from the explosive gas formation during the reduction reaction. This change in the pore volumes leads to a pore size diameter of $HrGO_{39MW}$ to 26.5 nm, where pore sizes of all other samples remained between 3 to 8 nm. These results indicate that the oxygen content of GO, the heating time, and heating speed should be chosen accordingly to optimize the pore volume distribution and the SSA by thermal treatment. Specifically, when oxygen content is low (14.4 wt.%), the heating time has more influence than heating speed, in contrast, when the oxygen content is high (39.1 wt%), the heating speed has more influence than heating time.

Taken together, precise control over rGO properties can be possible by simply designing the reduction routes. In other words, performing the same reduction on rGOs lead to different results when different oxygen content rGOs are used.

## 3.2 Lithium-ion battery application

### 3.2.1 Half-cell study.

The characteristics and performances of anode materials were assessed by a constant charge-discharge test in half cell vs. $Li^+/Li$. Based on the theoretical capacity of graphite, the current rate was fixed as 1C = 372 mA $g^{-1}$, and the voltage window was fixed between 0.01 V and 3.0 V to realize complete discharge and charge of lithium into the carbon host. In Fig. 2a, the charge-discharge behavior of $HrGO_{14T}$ is displayed. $HrGO_{14T}$ and other rGOs (Supplementary Fig. S7) show typical adsorption behavior. This behavior transcribes the change from battery to capacitor behavior from graphite to rGOs through the oxidation-reduction processes. The rate performances (Fig. 2b and 2c) present the consecutive charge response for 5 cycles from 1C to 100C. It demonstrates that all samples, except $HrGO_{39}$, have improved capacity compared to the theoretical capacity of graphite. This first difference highlights the improvement of capacity from graphite to rGOs as a result of lithium storage on both sides of graphene layers and internal spaces. Thus, the results for rGOs present an improved capacity as the SSA and the conductivity increase, reaching the capacity of 507 and 629 mAh $g^{-1}$ at 1C for $HrGO_{14T}$ and $HrGO_{39MW}$, respectively. At 20C, their capacity decreased to 186 and 281 mAh $g^{-1}$ for $HrGO_{14T}$ and $HrGO_{39MW}$. These results indicate the higher capacity and the superior rate capability of $HrGO_{14T}$ and $HrGO_{39MW}$. The cyclability of $HrGO_{14T}$ and $HrGO_{39MW}$ were evaluated over 500 cycles at 5C (Fig. 2d and Supplementary Fig. S8), expressing good stability and excellent coulombic efficiency among all. The charge-discharge cycling of as-prepared carbon materials showed three phases; at first, the capacity decreased until the 20th and 70th cycles, then increased until the 420th and 399th cycles, and finally decreased for $HrGO_{14T}$ and $HrGO_{39MW}$, respectively.

Next, the potential was plotted against the differential capacity (Fig. 2e and Supplementary Fig. S9, S10). The storage mechanism of lithium by graphene analogs can be divided from 0.01 V to 0.7 V and from 0.7 V to 3.0 V between the lithium intercalation/deintercalation occurring in graphene inter-layer and the lithium adsorption/desorption and redox reactions occurring on the graphene surface, respectively. In Fig. 2f (Supplementary Fig. S11, S12), the capacity evolution above and below 0.7 V is presented. Bellow 0.7 V, all graphene samples expressed an increase and decrease in their deintercalation behavior, originating from graphene interlayer wetting with the electrolyte and the formation of the solid electrolyte interface (SEI) formation, respectively. The SEI is formed by the decomposition of the solvent and lithium salt into a protective layer between the active material and the electrolyte.[44] The SEI hiders the diffusion of $Li^+$ and isolates graphene from the electrode and the electrolyte leading to reduced performance. The SEI is mostly generated from the initial discharge process and is sensitive to graphene size, edge to basal plan ratio, pore size, and surface composition. Wetting electrode materials also leads to form SEI, and graphene volume change induces stress leading to the SEI crack and reformation.[45] Above 0.7 V, all graphene samples showed three successive phases: 1) a decrease corresponding to the fading of oxygen redox reactions at 1.2 V, 1.8 V, and 2.5 V related to graphene carbonyl oxygen functional groups; 2) an increase corresponding to the wetting of graphene by the electrolyte resulting in an increased active surface; 3) a decrease originating from the continuous SEI formation isolating graphene from the electrode and the electrolyte. The maximum desorption capacity performances of graphene analogs are observed to correlate with their SSA (Supplementary Figure S9). The HrGOs results indicate that chemical reduction improves both the deintercalation and desorption behaviors by removing oxygen functional groups from its interlayer and surface (Supplementary Fig. S10a,S11a,S12a,S13a). Furthermore, compared with thermally reduced samples, chemically reduced HrGOs did not present any increase of capacity related to the $Li^+$ desorption denoting the fasten of SEI formation from excess oxygen functional groups. For $HrGO_{14}$, the tube furnace reduction method improved the intercalation and adsorption behavior, while the microwave method improved the intercalation behavior partially and only stabilized the adsorption behavior (Supplementary Fig. S10,S12). Compared with $HrGO_{14}$ (SSA of 217 $m^2$ $g^{-1}$ and oxygen content of 14 wt.%), $HrGO_{14MW}$ has a similar wrinkled 2D structure (Supplementary Figure S3f, S4f), superior SSA (333 $m^2$ $g^{-1}$), and lower oxygen content (6.5 wt.%). These differences demonstrate that the capacity is related to the SSA and that a large amount of oxygen tends to reduce LIBs stability. Compared with $HrGO_{14MW}$, $HrGO_{14T}$ has an identical wrinkled 2D structure (Supplementary Figure S3e, S4e), similar oxygen content (5.5 wt.%), and larger SSA (422 $m^2$ $g^{-1}$). These differences confirm that the capacity correlates with the SSA and that small oxygen content difference has a limited effect on LIBs stability.

Above chemical and morphological analysis of $HrGO_{14x}$ revealed the decrease of the oxygen content and the increase of SSA and micropore amount, which are responsible for the superior capacity performance of $HrGO_{14T}$ over $HrGO_{14MW}$. For $HrGO_{39}$, the tube furnace heating reduction method improved the intercalation and the adsorption behavior, while the microwave method improved the intercalation behavior and, more drastically, the adsorption behavior (Supplementary Fig. S11,S13). Compared with $HrGO_{39}$ (SSA of 88 $m^2$ $g^{-1}$ and oxygen content of 39 wt.%), $HrGO_{39T}$ has a similar flat 2D structure (Supplementary Figure S3b, S4b), SSA (93 $m^2$

$g^{-1}$), and lower oxygen content (2.9 wt.%). These differences result in a slight improvement in capacity and a clear improvement in stability, highlighting that a large amount of oxygen tends to reduce LIBs stability. Compared with $HrGO_{39T}$, $HrGO_{39MW}$ has similar oxygen content (4.8 wt.%), an original wrinkled 2D structure (Supplementary Figure S3c, S4c), and a larger SSA (532 $m^2$ $g^{-1}$). These differences indicate that the capacity is drastically improved by forming a wrinkled 2D structure as it leads to superior SSA, and that small oxygen content difference has a limited effect on graphene LIBs stability. According to the chemical and morphological analyses, the superior performance of $HrGO_{39MW}$ is due to its low oxygen content, which reduces SEI formation, superior SSA, which increase intercalation and adsorption behaviors, and original macropores corresponding to 6 times more pore volume compared with $HrGO_{14T}$, which is correlated with the drastic increase of the absorption capacity. Furthermore, among all samples, $HrGO_{39MW}$ expressed significant fluctuation in its capacity through cycling despite that it showed the highest capacity; this phenomenon might be related to the large pore volume and diameter of $HrGO_{39MW}$, which accelerates its wetting rate and SEI formation, leading to a faster active surface increase and decrease, respectively.

These results indicate that in order to produce the best rGO for LIBs in terms of capacity, rate capability, and cyclability; rGO should be synthesized from GO at its highest oxygen level, the reduction steps should start with a fast temperature increase, to exfoliate graphene layers taking advantage of oxygen functional groups decomposition, and maintain this high temperature to remove residual oxygen functional groups. As obtained rGO will display high SSA, high conductivity, and low oxygen content, which respectively mainly influence rGO capacity, capability, and stability.

### 3.2.2 Full-cell study.

Convinced by the above results, we decided to assemble a full-cell combining $HrGO_{39MW}$, and our previously reported BTO-LCO as a cathode (Supplementary Fig. S14). We expected that both of these high rate capability materials hold great promises for high rate capability full-cell LIBs system. In order to build a full-cell system, irreversible consumption of lithium upon cycling must be considered since the lithium amount is limited in the full-cell; in the case of a half-cell, excess lithium can be supplied from the counter Li electrode.[45] The lithium consumption can be caused by (1) the SEI formation and (2) the additional SEI formation at the cracks upon charge/discharge cycle. As for cathode, BTO-LCO suppresses the formation of native SEI at a triple-phase junction, where the redox reaction actively occurs.[24,25] However, prepared graphene analogs suffer from large irreversible lithium consumption upon the first lithiation process, which correlates with their

SSA (Supplementary Table S2 and Figure S15). To overcome this problem, we investigated several pre-lithiation methods; chemical pre-lithiation, electrochemical pre-lithiation, and direct contact pre-lithiation (DCPL).[46–48] Compared with chemical and electrochemical pre-lithiation; DCPL is fast, easy, and scalable. For these reasons, DCPL was applied to our rGOs (Fig. 3a). The DCPL was performed by pressing the anode and lithium foil in the presence of 1 M $L^{-1}$ $LiPF_6$ dissolved in a mixture of ethylene carbonate (EC) and diethyl carbonate (DEC) (v/v, 3/7). By using the $LIPF_6$ electrolyte, we consider a flow of electron is created due to the difference of potential between the active anode material and the lithium foil.[46–48] In order to control and optimize the DCPL, a time study was conducted (Supplementary Fig. S16). The results showed that as the DCPL time increases, more lithium is absorbed into the carbon electrode, decreasing its half-cell initial potential. The DCPL was continued until potential values were stabilized (state of charge (SOC) of 50%). In the case of graphite after only 15 min of DCPL, the potential stabilized at 100 mV, indicating complete pre-lithiation, and while for $HrGO_{39MW}$, the pre-lithiation required 2 hours to reach a stable value of 250 mV. The lithiation of the graphite electrode was visually recognizable; changing color from black to yellow (Fig.3a). The progress of graphite lithiation was also confirmed by XRD; its original structure showed a peak at 26.3°, while after DPCL, it displayed a mixture of graphite interacted compound stage 1 at 23.9° and stage 2 at 25.1° (Fig. 3b). The effect of DCPL on $HrGO_{39MW}$ anode half-cell was evaluated; as a result, the initial irreversible capacity decreased (Supplementary Table S3), and the SEI formation within 1.4 V to 1.0 V disappeared (Supplementary Fig. S17), indicating the successful SEI formation by our DCPL treatment.

In light of these positive results, full-cell was prepared by applying DCPL on anode material prior assembly. Two full-cells were assembled composed of a BTO-LCO cathode and a $HrGO_{39MW}$ anode using a capacity ratio of anode to cathode (N/P ratio) of 1.1 and 2.3, respectively named LC-$rGO_{1.1}$ and LC-$rGO_{2.3}$. The full-cells were evaluated at constant current at various current rate from 1C (1C = 160 mA $g^{-1}$) to 100C.

The results (Fig. 4a) show that both designs have similar capacity performances at 1C and 2C showing a capacity of 154 mAh $g^{-1}$. At higher current density LC-$rGO_{2.3}$ showed superior rate capability performance compared with LC-$rGO_{1.1}$, at 20C LC-$rGO_{2.3}$ showed 88 mAh $g^{-1}$ while LC-$rGO_{1.1}$ showed 10 mAh $g^{-1}$, corresponding to 56% and 6% capacity retention once compared with the maximum capacity at 1C. Furthermore, stability study indicated that LC-$rGO_{1.1}$ start fading after only 50 cycles (Fig. 4bi), while LC-$rGO_{2.3}$ remained stable even after 180 cycles (Fig. 4bii). All these results demonstrate the higher capacity, rate capability, and stability of LC-$rGO_{2.3}$ over LC-$rGO_{1.1}$. The poor stability and capability of lower N/P ratio LC-rGO might be due to the irreversible capacity consumption of rGO electrode from the

LC electrode, as in this configuration rGO volume deformation upon lithium absorption and desorption lead to higher mechanical stress and SEI cracking. Moreover, the charge-discharge behavior of LC-rGO$_{2.3}$ full-cell showed excellent battery behavior similar to BTO-LCO half-cell, displaying a flat charge-discharge plateau at 3.7 V (Fig. 4cii). Furthermore, LC-rGO$_{2.3}$ showed similar to better capacity performances compared with BTO-LCO cathode half-cell; at 50C, the full-cell shows 42 mAh g$^{-1}$ while the half-cell shows close to 0 mAh g$^{-1}$ (Supplementary Fig. S9). These results demonstrate the superiority of our pre-lithiated rGO over lithium foil, opening the door for higher rate performance LIBs. Compared with other recently reported metal oxide-based full-cells (Fig. 4d), our LC-rGO$_{2.3}$ battery showed excellent power and energy densities;[3,49–53] LC-rGO$_{2.3}$ delivered 604 Wh kg$^{-1}$ at 432 W kg$^{-1}$ and maintained 293 Wh kg$^{-1}$ at 8,658 W kg$^{-1}$ and 20 Wh kg$^{-1}$ at 43,333 W kg$^{-1}$.

## 4. Conclusions

In summary, the combination of chemical and thermal reduction process allows excellent control over rGO crystallinity, disorder, oxygen content, conductivity, and surface area. These differences are ascribed to the amount and speed of oxygen functional group decomposition. The application of as prepared rGOs toward half-cell LIBs technology reveals that the control of such reduction methods and thus control over rGO properties is a key to unlock high capacity, high rate capability, high stability anode materials. Furthermore, optimized rGO applied toward full-cell LIBs using our DCPL method allows perfect technology transfer from our previous high rate BTO-LCO cathode half-cell toward higher energy density and power density full-cell.

## Conflicts of interest

There are no conflicts to declare.

## Acknowledgements

We thank Satoshi Yasuno and the staff of SPring-8 for supporting the HAXPES experiments (Proposal Number: 2019A1778). We also thank Prof. Obata Seiji (Okayama University), Mylan Lam (Pierre and Marie Curie University), Valentin Barbe-Richaud (INP-Phelma). This research was supported by JST CREST (JPMJCR18R3).

## References

[1] M.S. Whittingham, Electrical Energy Storage and Intercalation Chemistry, Science. 192 (1976) 1126–1127. https://doi.org/10.1126/science.192.4244.1126.

[2] K. Mizushima, P.C. Jones, P.J. Wiseman, J.B. Goodenough, LixCoO2 (0, Mater. Res. Bull. 15 (1980) 783–789. https://doi.org/10.1016/0025-5408(80)90012-4.

[3] C. Wang, L. Wu, H. Wang, W. Zuo, Y. Li, J. Liu, Fabrication and Shell Optimization of Synergistic TiO2-MoO3 Core–Shell Nanowire Array Anode for High Energy and Power Density Lithium-Ion Batteries, Adv. Funct. Mater. 25 (2015) 3524–3533. https://doi.org/10.1002/adfm.201500634.

[4] X. Tang, G. Chen, Z. Mo, D. Ma, S. Wang, J. Wen, L. Gong, L. Zhao, J. Huang, T. Huang, J. Luo, Controllable two-dimensional movement and redistribution of lithium ions in metal oxides, Nat. Commun. 10 (2019) 2888. https://doi.org/10.1038/s41467-019-10875-w.

[5] X. Chen, H. Huang, L. Pan, T. Liu, M. Niederberger, Fully Integrated Design of a Stretchable Solid-State Lithium-Ion Full Battery, Adv. Mater. 0 (n.d.) 1904648. https://doi.org/10.1002/adma.201904648.

[6] X. Shen, Z. Cao, M. Chen, J. Zhang, D. Chen, A Novel Flexible Full-Cell Lithium Ion Battery Based on Electrospun Carbon Nanofibers Through a Simple Plastic Package, Nanoscale Res. Lett. 13 (2018). https://doi.org/10.1186/s11671-018-2788-7.

[7] X. Gao, F. Wang, S. Gollon, C. Yuan, Micro Silicon–Graphene–Carbon Nanotube Anode for Full Cell Lithium-ion Battery, J. Electrochem. Energy Convers. Storage. 16 (2018) 011009-011009–6. https://doi.org/10.1115/1.4040826.

[8] H. Xu, S. Li, C. Zhang, X. Chen, W. Liu, Y. Zheng, Y. Xie, Y. Huang, J. Li, Roll-to-roll prelithiation of Sn foil anode suppresses gassing and enables stable full-cell cycling of lithium ion batteries, Energy Environ. Sci. (2019). https://doi.org/10.1039/C9EE01404G.

[9] S.W. Lee, I. Ryu, W.D. Nix, Y. Cui, Fracture of crystalline germanium during electrochemical lithium insertion, Extreme Mech. Lett. 2 (2015) 15–19. https://doi.org/10.1016/j.eml.2015.01.009.

[10] Q. Zhang, H. Chen, L. Luo, B. Zhao, H. Luo, X. Han, J. Wang, C. Wang, Y. Yang, T. Zhu, M. Liu, Harnessing the concurrent reaction dynamics in active Si and Ge to achieve high performance lithium-ion batteries, Energy Environ. Sci. 11 (2018) 669–681. https://doi.org/10.1039/C8EE00239H.

[11] H. Fujimoto, K. Tokumitsu, A. Mabuchi, N. Chinnasamy, T. Kasuh, The anode performance of the hard carbon for the lithium ion battery derived from the oxygen-containing aromatic precursors, J. Power Sources. 195 (2010) 7452–7456. https://doi.org/10.1016/j.jpowsour.2010.05.041.

[12] H. Tian, F. Xin, X. Wang, W. He, W. Han, High capacity group-IV elements (Si, Ge, Sn) based anodes for lithium-ion batteries, J. Materiomics. 1 (2015) 153–169. https://doi.org/10.1016/j.jmat.2015.06.002.

[13] X.H. Liu, L. Zhong, S. Huang, S.X. Mao, T. Zhu, J.Y. Huang, Size-Dependent Fracture of Silicon Nanoparticles During Lithiation, ACS Nano. 6 (2012) 1522–1531. https://doi.org/10.1021/nn204476h.

[14] E. Yoo, J. Kim, E. Hosono, H. Zhou, T. Kudo, I. Honma, Large Reversible Li Storage of Graphene Nanosheet Families for Use in Rechargeable Lithium Ion Batteries, Nano Lett. 8 (2008) 2277–2282. https://doi.org/10.1021/nl800957b.

[15] Z. Gao, W. Yang, J. Wang, N. Song, X. Li, Flexible all-solid-state hierarchical NiCo2O4/porous graphene paper asymmetric supercapacitors with an exceptional combination of electrochemical properties, Nano Energy. 13 (2015) 306–317. https://doi.org/10.1016/j.nanoen.2015.02.036.

[16] Z. Gao, N. Song, X. Li, Microstructural design of hybrid CoO@NiO and graphene nano-architectures for flexible high performance supercapacitors, J. Mater. Chem. A. 3 (2015) 14833–14844. https://doi.org/10.1039/C5TA03057A.

[17] Y. Zhang, Z. Gao, X. Li, Capillarity Composited Recycled Paper/Graphene Scaffold for Lithium–Sulfur Batteries with Enhanced Capacity and Extended Lifespan, Small. 13 (2017) 1701927. https://doi.org/10.1002/smll.201701927.

[18] Y. Zhang, Z. Gao, N. Song, J. He, X. Li, Graphene and its derivatives in lithium–sulfur batteries, Mater. Today Energy. 9 (2018) 319–335. https://doi.org/10.1016/j.mtener.2018.06.001.

[19] J. Cho, Y.J. Kim, B. Park, Novel LiCoO2 Cathode Material with Al2O3 Coating for a Li Ion Cell, Chem. Mater. 12 (2000) 3788–3791. https://doi.org/10.1021/cm000511k.

[20] J. Cho, Y.J. Kim, B. Park, LiCoO2 Cathode Material That Does Not Show a Phase Transition from Hexagonal to Monoclinic Phase, J. Electrochem. Soc. 148 (2001) A1110–A1115. https://doi.org/10.1149/1.1397772.

[21] I.D. Scott, Y.S. Jung, A.S. Cavanagh, Y. Yan, A.C. Dillon, S.M. George, S.-H. Lee, Ultrathin Coatings on Nano-LiCoO2 for Li-Ion Vehicular Applications, Nano Lett. 11 (2011) 414–418. https://doi.org/10.1021/nl1030198.

[22] Y.S. Jung, A.S. Cavanagh, A.C. Dillon, M.D. Groner, S.M. George, S.-H. Lee, Enhanced Stability of LiCoO2 Cathodes in Lithium-Ion Batteries Using Surface Modification by Atomic Layer Deposition, J. Electrochem. Soc. 157 (2010) A75–A81. https://doi.org/10.1149/1.3258274.

[23] T. Teranishi, Y. Yoshikawa, M. Yoneda, A. Kishimoto, J. Halpin, S. O'Brien, M. Modreanu, I.M. Povey, Aluminum Interdiffusion into LiCoO2 Using Atomic Layer Deposition for High Rate Lithium Ion Batteries, ACS Appl. Energy Mater. 1 (2018) 3277–3282. https://doi.org/10.1021/acsaem.8b00496.

[24] T. Teranishi, Y. Yoshikawa, R. Sakuma, H. Hashimoto, H. Hayashi, A. Kishimoto, T. Fujii, High-rate performance of ferroelectric BaTiO3-coated LiCoO2 for Li-ion batteries, Appl. Phys. Lett. 105 (2014) 143904. https://doi.org/10.1063/1.4898006.

[25] T. Teranishi, N. Katsuji, K. Chajima, S. Yasuhara, M. Inohara, Y. Yoshikawa, S. Yasui, H. Hayashi, A. Kishimoto, M. Itoh, Low-Temperature High-Rate Capabilities of Lithium Batteries via Polarization-Assisted Ion Pathways, Adv. Electron. Mater. 4 (2018) 1700413. https://doi.org/10.1002/aelm.201700413.

[26] X. Cai, L. Lai, Z. Shen, J. Lin, Graphene and graphene-based composites as Li-ion battery electrode materials and their application in full cells, J. Mater. Chem. A. 5 (2017) 15423–15446. https://doi.org/10.1039/C7TA04354F.

[27] W.L. Ripeng Luo, W.L. Ripeng Luo, Overview of Graphene as Anode in Lithium-ion Batteries, J. Electron. Sci. Technol. (n.d.) 1–12. https://doi.org/10.11989/JEST.1674-862X.6032519.

[28] X. Zhu, Y. Zhu, S. Murali, M.D. Stoller, R.S. Ruoff, Nanostructured Reduced Graphene Oxide/Fe2O3 Composite As a High-Performance Anode Material for Lithium Ion Batteries, ACS Nano. 5 (2011) 3333–3338. https://doi.org/10.1021/nn200493r.

[29] N. Morimoto, T. Kubo, Y. Nishina, Tailoring the Oxygen Content of Graphite and Reduced Graphene Oxide for Specific Applications, Sci. Rep. 6 (2016) 21715. https://doi.org/10.1038/srep21715.

[30] S. Stankovich, D.A. Dikin, R.D. Piner, K.A. Kohlhaas, A. Kleinhammes, Y. Jia, Y. Wu, S.T. Nguyen, R.S. Ruoff, Synthesis of graphene-based nanosheets via chemical reduction of exfoliated graphite oxide, Carbon. 45 (2007) 1558–1565. https://doi.org/10.1016/j.carbon.2007.02.034.

[31] M.C. Kim, G.S. Hwang, R.S. Ruoff, Epoxide reduction with hydrazine on graphene: A first principles study, J. Chem. Phys. 131 (2009) 064704. https://doi.org/10.1063/1.3197007.

[32] S. Park, Y. Hu, J.O. Hwang, E.-S. Lee, L.B. Casabianca, W. Cai, J.R. Potts, H.-W. Ha, S. Chen, J. Oh, S.O. Kim, Y.-H. Kim, Y. Ishii, R.S. Ruoff, Chemical structures of hydrazine-treated graphene oxide and generation of aromatic nitrogen doping, Nat. Commun. 3 (2012) 1–8. https://doi.org/10.1038/ncomms1643.

[33] C.K. Chua, M. Pumera, Chemical reduction of graphene oxide: a synthetic chemistry viewpoint, Chem. Soc. Rev. 43 (2013) 291–312. https://doi.org/10.1039/C3CS60303B.

[34] H.C. Schniepp, J.-L. Li, M.J. McAllister, H. Sai, M. Herrera-Alonso, D.H. Adamson, R.K. Prud'homme, R. Car, D.A. Saville, I.A. Aksay, Functionalized Single Graphene Sheets Derived

from Splitting Graphite Oxide, J. Phys. Chem. B. 110 (2006) 8535–8539. https://doi.org/10.1021/jp060936f.

[35] Z.-S. Wu, W. Ren, L. Gao, J. Zhao, Z. Chen, B. Liu, D. Tang, B. Yu, C. Jiang, H.-M. Cheng, Synthesis of Graphene Sheets with High Electrical Conductivity and Good Thermal Stability by Hydrogen Arc Discharge Exfoliation, ACS Nano. 3 (2009) 411–417. https://doi.org/10.1021/nn900020u.

[36] M.J. McAllister, J.-L. Li, D.H. Adamson, H.C. Schniepp, A.A. Abdala, J. Liu, M. Herrera-Alonso, D.L. Milius, R. Car, R.K. Prud'homme, I.A. Aksay, Single Sheet Functionalized Graphene by Oxidation and Thermal Expansion of Graphite, Chem. Mater. 19 (2007) 4396–4404. https://doi.org/10.1021/cm0630800.

[37] L. Stobinski, B. Lesiak, A. Malolepszy, M. Mazurkiewicz, B. Mierzwa, J. Zemek, P. Jiricek, I. Bieloshapka, Graphene oxide and reduced graphene oxide studied by the XRD, TEM and electron spectroscopy methods, J. Electron Spectrosc. Relat. Phenom. 195 (2014) 145–154. https://doi.org/10.1016/j.elspec.2014.07.003.

[38] A.C. Ferrari, D.M. Basko, Raman spectroscopy as a versatile tool for studying the properties of graphene, Nat. Nanotechnol. 8 (2013) 235–246. https://doi.org/10.1038/nnano.2013.46.

[39] S. Pei, H.-M. Cheng, The reduction of graphene oxide, Carbon. 50 (2012) 3210–3228. https://doi.org/10.1016/j.carbon.2011.11.010.

[40] S. Gadipelli, Z.X. Guo, Graphene-based materials: Synthesis and gas sorption, storage and separation, Prog. Mater. Sci. 69 (2015) 1–60. https://doi.org/10.1016/j.pmatsci.2014.10.004.

[41] B. Diby Ossonon, D. Bélanger, Synthesis and characterization of sulfophenyl-functionalized reduced graphene oxide sheets, RSC Adv. 7 (2017) 27224–27234. https://doi.org/10.1039/C6RA28311J.

[42] T. Miyata, S. Gohda, T. Fujii, H. Ono, H. Itoh, Y. Nishina, K. Kashimura, Pure electric and magnetic fields applied to reduced graphene oxide for defect repair and oxygen removal, Carbon. 171 (2021) 10–15. https://doi.org/10.1016/j.carbon.2020.08.044.

[43] N. Morimoto, H. Suzuki, Y. Takeuchi, S. Kawaguchi, M. Kunisu, C.W. Bielawski, Y. Nishina, Real-Time, in Situ Monitoring of the Oxidation of Graphite: Lessons Learned, Chem. Mater. 29 (2017) 2150–2156. https://doi.org/10.1021/acs.chemmater.6b04807.

[44] R. Mukherjee, A.V. Thomas, A. Krishnamurthy, N. Koratkar, Photothermally Reduced Graphene as High-Power Anodes for Lithium-Ion Batteries, ACS Nano. 6 (2012) 7867–7878. https://doi.org/10.1021/nn303145j.

[45] S.J. An, J. Li, C. Daniel, D. Mohanty, S. Nagpure, D.L. Wood, The state of understanding of the lithium-ion-battery graphite solid electrolyte interphase (SEI) and its relationship to formation cycling, Carbon. 105 (2016) 52–76. https://doi.org/10.1016/j.carbon.2016.04.008.

[46] H. Park, M. Kim, F. Xu, C. Jung, S.M. Hong, C.M. Koo, In situ synchrotron wide-angle X-ray scattering study on rapid lithiation of graphite anode via direct contact method for Li-ion capacitors, J. Power Sources. 283 (2015) 68–73. https://doi.org/10.1016/j.jpowsour.2015.01.193.

[47] F. Holtstiege, P. Bärmann, R. Nölle, M. Winter, T. Placke, Pre-Lithiation Strategies for Rechargeable Energy Storage Technologies: Concepts, Promises and Challenges, Batteries. 4 (2018) 4. https://doi.org/10.3390/batteries4010004.

[48] A. Shellikeri, V.G. Watson, D.L. Adams, E.E. Kalu, J.A. Read, T.R. Jow, J.P. Zheng, Pre-Lithiation of Carbon Anodes Using Different Lithium - Sources, ECS Trans. 77 (2017) 293–303. https://doi.org/10.1149/07711.0293ecst.

[49] Y. Yu, S. Huang, B. Wang, D. Tie, Q. Wang, Y. Hou, Y. Zhao, Achieving High-Energy Full-Cell Lithium-Storage Performance by Coupling High-Capacity V2O3 with Low-Potential Ni2P Anode, ACS Appl. Mater. Interfaces. 11 (2019) 19–25. https://doi.org/10.1021/acsami.8b17910.

[50] Z. Fang, J. Peng, N. Ma, L. Liang, H. Gao, H. Zhou, X. Jin, J. Yang, M. Liu, J. Du, Q. Li, X. Li, L. Li, Preparation and Optimization of New High-Power Nanoscale Li4Ti5O12 Full-Cell System, J. Nanosci. Nanotechnologie. 18 (2018) 8232–8239. https://doi.org/doi/10.1166/jnn.2018.16385.

[51] H. Ming, J. Ming, S.-M. Oh, E.-J. Lee, H. Huang, Q. Zhou, J. Zheng, Y.-K. Sun, High dispersion of TiO2 nanocrystals within porous carbon improves lithium storage capacity and can be applied batteries to LiNi0.5Mn1.5O4, J. Mater. Chem. A. 2 (2014) 18938–18945. https://doi.org/10.1039/C4TA03557G.

[52] H. Sun, X. He, J. Ren, J. Li, C. Jiang, C. Wan, Hard carbon/lithium composite anode materials for Li-ion batteries, Electrochimica Acta. 52 (2007) 4312–4316. https://doi.org/10.1016/j.electacta.2006.12.012.

[53] Z. Sun, Z. Li, X.-L. Wu, M. Zou, D. Wang, Z. Gu, J. Xu, Y. Fan, S. Gan, D. Han, L. Niu, A Practical Li-Ion Full Cell with a High-Capacity Cathode and Electrochemically Exfoliated Graphene Anode: Superior Electrochemical and Low-Temperature Performance, ACS Appl. Energy Mater. 2 (2019) 486–492. https://doi.org/10.1021/acsaem.8b01524.

# Table and Figure captions

Table 1: Effect of thermally induced CO and CO2, SSA, pore volume, pore size, and conductivity of rGOs.

Fig. 1 - Characterization of (i) GO, (ii) $HrGO_{39}$, (iii) $HrGO_{39T}$, (iv) $HrGO_{39MW}$, (v) $HrGO_{14}$, (vi) $HrGO_{14T}$, (vii) $HrGO_{14MW}$. (a) XRD, (b) RAMAN spectroscopy, (c) TEM of HrGO14T, (d) XPS C1s narrow scan. Isothermal $N_2$ absorption-desorption of (e) $HrGO_{39}$s and (f) $HrGO_{14}$s.

Fig. 2 - Half-cell lithium ion battery results of (i) $HrGO_{39}$, (ii) $HrGO_{39T}$, (iii) $HrGO_{39MW}$, (iv) $HrGO_{14}$, (v) $HrGO_{14T}$, (vi) $HrGO_{14MW}$. (a) galvanostatic charge discharge behavior, (b) and (c) rate capacity performances, (d) cycling performances and coulombic efficiency, (e) differential capacity plot of $HrGO_{39MW}$, (f) Capacity evolution above and below 0.7 V of $HrGO_{39MW}$.

Fig. 3 - (a) Illustration and digital images of DCPL treatment, and (b) ex-situ XRD of pre-lithiated graphite electrode.

Fig. 4: Full-cell lithium-ion battery results of LC-rGO with N/P equal to (i) 1.1, (ii) 2.3. (a) Full-cell rate performances, (c) Full-cell cyclability at 1C, (c) full-cell galvanostatic charge-discharge behavior, (d) Ragone plots of lithium metal oxide full-cell.

## Table 1

| **Reducing method** | **Hydrazine** 62.5 µL g$^{-1}$ | | | **Hydrazine** 1 mL g$^{-1}$ | | |
|---|---|---|---|---|---|---|
| | | **Tube furnace** | **Microwave** | | **Tube furnace** | **Microwave** |
| **Sample name** | **HrGO$_{39}$** | **HrGO$_{39T}$** | **HrGO$_{39MW}$** | **HrGO$_{14}$** | **HrGO$_{14T}$** | **HrGO$_{14MW}$** |
| Effect of thermally induced CO and CO$_2$ | - | rGO decomposition | rGO exfoliation | - | Low | Low |
| Oxygen wt% | 39.07 | 2.87 | 4.77 | 14.42 | 5.49 | 6.52 |
| SSA (m$^2$ g$^{-1}$) | 88 | 93 | 532 | 217 | 422 | 333 |
| Pore diameter (nm) | 3.5 | 5.2 | 26.5 | 6.8 | 6.7 | 7.4 |
| Pore Volume (cm$^3$ g$^{-1}$) | 5.7 10$^{-2}$ | 0.111 | 3.512 | 0.354 | 0.662 | 0.592 |
| Conductivity (S m$^{-1}$) | 7.7 10$^{-2}$ | 5.6 10$^3$ | 4.0 10$^2$ | 2.1 10$^3$ | 4.4 10$^3$ | 1.7 10$^3$ |

## Figure 1

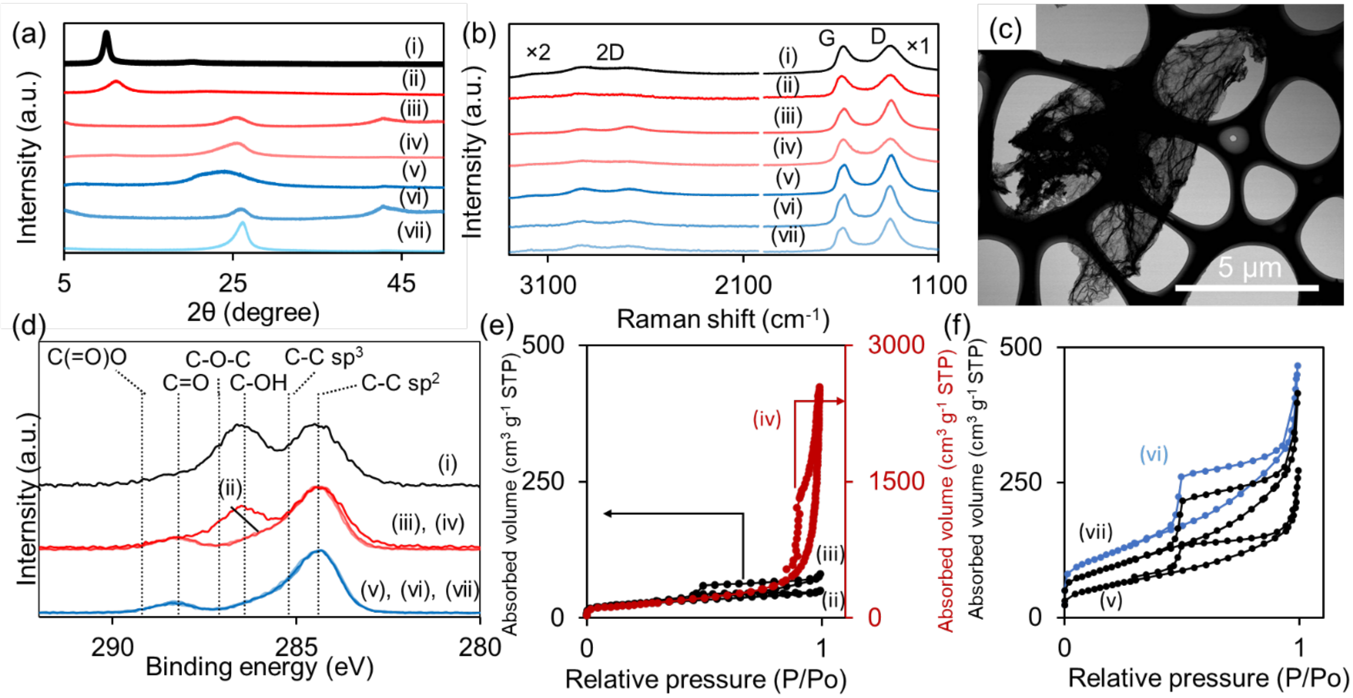
(a)
Intensity (a.u.)
(i)
(ii)
(iii)
(iv)
(v)
(vi)
(vii)
5
25
45
2θ (degree)
(b)
Intensity (a.u.)
×2
2D
G
D
×1
(i)
(ii)
(iii)
(iv)
(v)
(vi)
(vii)
3100
2100
1100
Raman shift (cm$^{-1}$)
(c)
5 µm
(d)
Intensity (a.u.)
C(=O)O
C=O
C-O-C
C-OH
C-C sp$^3$
C-C sp$^2$
(i)
(ii)
(iii), (iv)
(v), (vi), (vii)
290
285
280
Binding energy (eV)
(e)
Absorbed volume (cm$^3$ g$^{-1}$ STP)
500
250
0
(iv)
(iii)
(ii)
Absorbed volume (cm$^3$ g$^{-1}$ STP)
3000
1500
0
0
1
Relative pressure (P/Po)
(f)
Absorbed volume (cm$^3$ g$^{-1}$ STP)
500
250
0
(vi)
(vii)
(v)
0
1
Relative pressure (P/Po)

# Figure 2

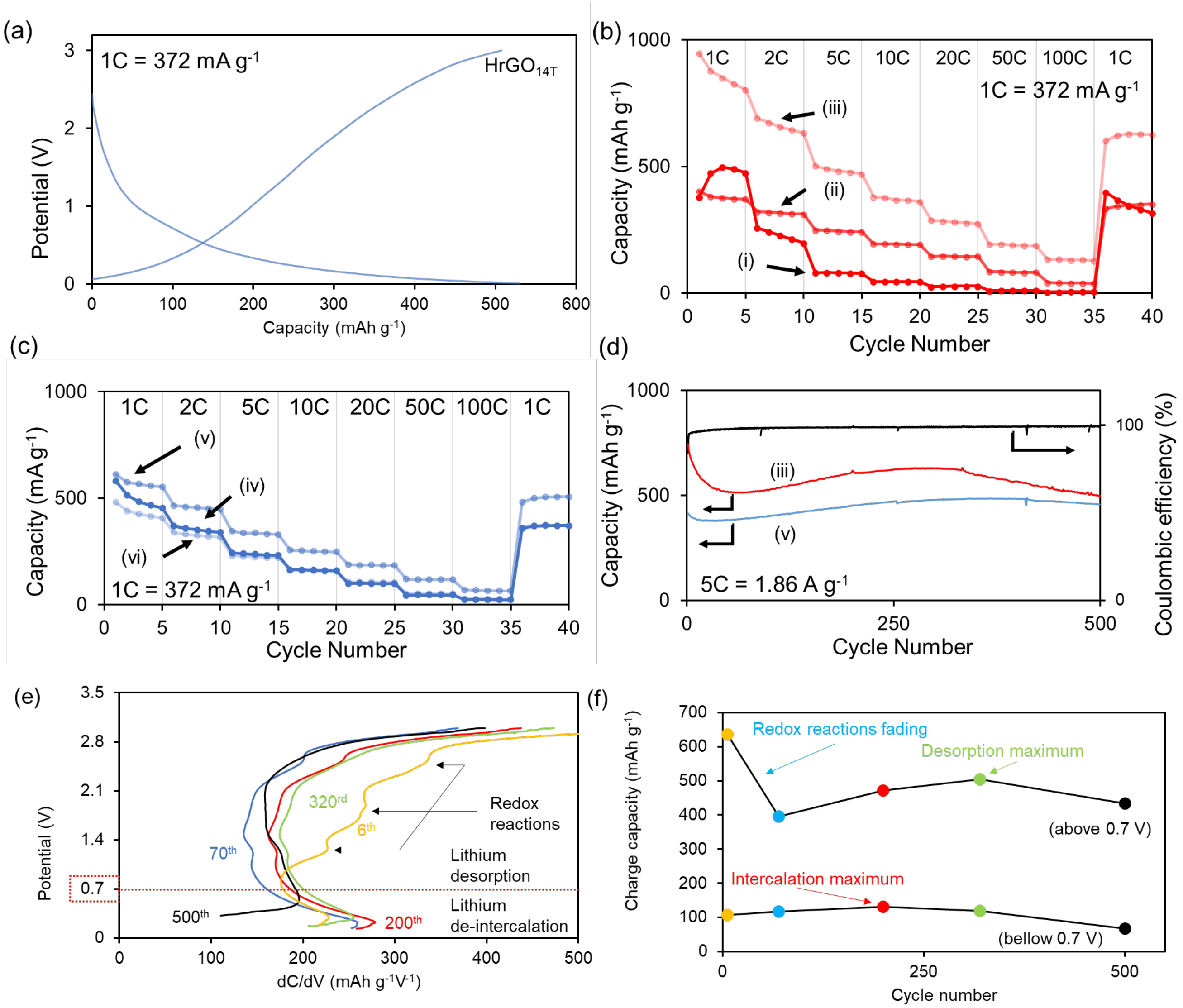

# Figure 3

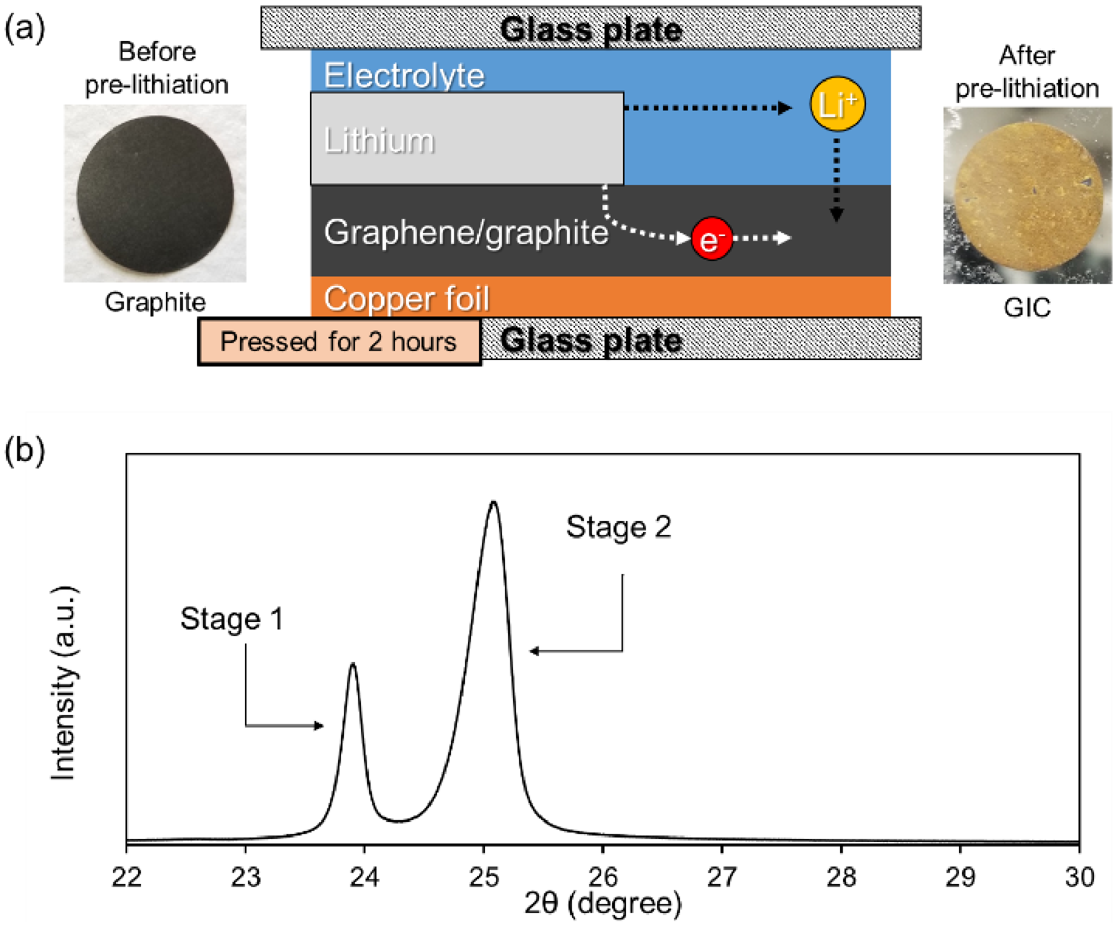
(a)
Before pre-lithiation
Graphite
Glass plate
Electrolyte
Lithium
Li+
Graphene/graphite
e-
Copper foil
Pressed for 2 hours
Glass plate
After pre-lithiation
GIC
(b)
Intensity (a.u.)
Stage 1
Stage 2
22
23
24
25
26
27
28
29
30
2θ (degree)

# Figure 4

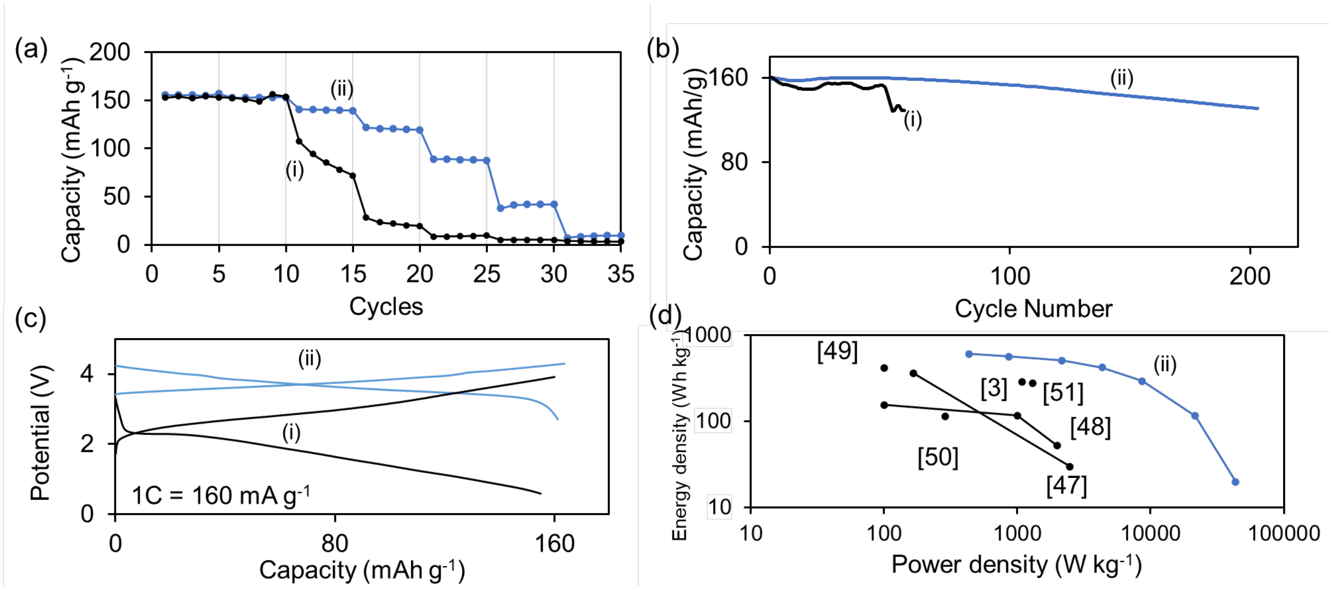
(a)
Capacity (mAh g-1)
200
150
100
50
0
(ii)
(i)
0
5
10
15
20
25
30
35
Cycles
(b)
Capacity (mAh/g)
160
80
0
(ii)
(i)
0
100
200
Cycle Number
(c)
Potential (V)
4
2
0
(ii)
(i)
1C = 160 mA g-1
0
80
160
Capacity (mAh g-1)
(d)
Energy density (Wh kg-1)
1000
100
10
[49]
[3]
[51]
[48]
[50]
[47]
(ii)
10
100
1000
10000
100000
Power density (W kg-1)

# Highlights :

- Combine chemical and thermal reduction methods were employed for the synthesis or reduce graphene oxide.
- Best reduced graphene oxide material for LIBs was prepared via combined small chemical reduction and fast heating thermal reduction.
- Best reduced graphene oxide shows 947 mAh $g^{-1}$ at 372 mA $g^{-1}$.
- Correlation of behavior was observed between SSA and capacity, conductivity and capability, and oxygen level and cyclability.
- High-rate full-cell LIBs was assembled using $LiCoO_2$@$BaTiO_3$ cathode and our optimized rGO anode displaying high energy and power density, 293 Wh $kg^{-1}$ at 8,658 W $kg^{-1}$.